NANO LETTERS

pubs.acs.org/NanoLett Letter

Long-Lived Phonon Polaritons in Hyperbolic Materials

Guangxin Ni,* Alexander S. McLeod, Zhiyuan Sun, Joseph R. Matson, Chiu Fan Bowen Lo, Daniel A. Rhodes, Francesco L. Ruta, Samuel L. Moore, Rocco A. Vitalone, Ramon Cusco, Luis Artús, Lin Xiong, Cory R. Dean, James C. Hone, Andrew J. Millis, Michael M. Fogler, James H. Edgar, Joshua D. Caldwell, and D. N. Basov*

Cite This: *Nano Lett.* 2021, 21, 5767−5773 Read Online

ACCESS | Metrics & More | Article Recommendations | Supporting Information

ABSTRACT: Natural hyperbolic materials with dielectric permittivities of opposite signs along different principal axes can confine long-wavelength electromagnetic waves down to the nanoscale, well below the diffraction limit. Confined electromagnetic waves coupled to phonons in hyperbolic dielectrics including hexagonal boron nitride (hBN) and α-MoO_3 are referred to as hyperbolic phonon polaritons (HPPs). HPP dissipation at ambient conditions is substantial, and its fundamental limits remain unexplored. Here, we exploit cryogenic nanoinfrared imaging to investigate propagating HPPs in isotopically pure hBN and naturally abundant α-MoO_3 crystals. Close to liquid-nitrogen temperatures, losses for HPPs in isotopic hBN drop significantly, resulting in propagation lengths in excess of 8 μm, with lifetimes exceeding 5 ps, thereby surpassing prior reports on such highly confined polaritonic modes. Our nanoscale, temperature-dependent imaging reveals the relevance of acoustic phonons in HPP damping and will be instrumental in mitigating such losses for miniaturized mid-infrared technologies operating at liquid-nitrogen temperatures.

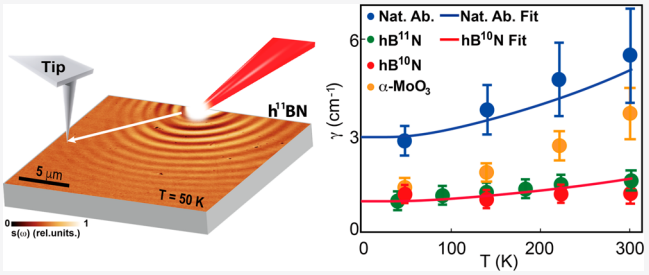

KEYWORDS: *phonon polaritons, hyperbolic materials, nanoinfrared imaging, van der Waals heterostructures*

We investigate hyperbolic phonon polariton (HPP) propagation and dissipation in isotopically pure hexagonal boron nitride ($h^{10}BN$, $h^{11}BN$), along with naturally abundant hBN and α-MoO_3 van der Waals crystals using near-field infrared (IR) microscopy. Nano-IR methods allow one to directly visualize polaritonic standing waves on the surfaces of these hyperbolic materials.[1−7] Similar to graphene plasmon polariton investigations,[8−13] both the wavelength of the HPP $\lambda_p(\omega)$ and its dissipation γ can be readily obtained from nano-IR images (Figures 1 and 2), with these two quantities allowing one to extract the complex dielectric function $\varepsilon(\omega) = \varepsilon' + i\varepsilon''$ of a phononic medium.[3−6] Earlier attempts have characterized HPPs in isotopically pure hBN ($h^{10}BN$, $h^{11}BN$) and in α-MoO_3 crystals at ambient conditions.[6,14−19] However, the fundamental limits of HPP dissipation and lifetime remain to be determined as this necessarily relies on temperature-dependent nanoimaging of polaritonic waves. In this work, we report cryogenic nanoimaging results of these van der Waals materials for the first time, demonstrating record-long HPP lifetimes. We studied isotopically pure hBN and biaxial hyperbolic α-MoO_3 crystals and compared these results with naturally abundant hBN crystals. Combined with theoretical models, we examined the physics governing HPP dissipation in isotopically pure hyperbolic crystals.

To perform cryogenic nanoimaging, we utilized a home-built scanning near-field IR microscope operating at variable temperatures.[8,20−22] In this setup, the incident light with IR frequency ω is focused onto the metallized tip of an atomic force microscope (AFM). As the tip approaches the sample, a concentrated evanescent field excites polaritonic modes with a $\lambda_p(\omega)$ that is much shorter than the free-space wavelength $\lambda_{IR} = 2\pi c/\omega$ of the incident photons.[23−27] This unique nano-IR apparatus has been routinely employed in studies of plasmon and phonon polaritons as well as for visualizing inhomogeneities in complex oxides.[20−22] In the previous HPP nanoimaging studies, a physical sample edge was chosen as the HPP wave reflector,[6] resulting in the imaging of coexisting fringes with two distinct periodicities λ_p and $\lambda_p/2$. To avoid the complications of λ_p and $\lambda_p/2$ fringe decompositions, an alternative approach is preferred. In our device (Figure 1b), prepatterned micron-sized Au disk structures residing on top of the hBN crystals (bottom of α-MoO_3) serve as fixed HPP antennas (Figures 1 and 2) predominantly producing fringes with λ_p periodicity.

Received: April 20, 2021
Revised: June 8, 2021
Published: June 18, 2021

https://doi.org/10.1021/acs.nanolett.1c01562
Nano Lett. 2021, 21, 5767−5773

a

	hBN			α-MoO_3		
Hyperbolic Bands (cm^{-1})	$\varepsilon_x = \varepsilon_y > 0$, $\varepsilon_z < 0$	$\varepsilon_x = \varepsilon_y < 0$, $\varepsilon_z > 0$		$\varepsilon_x, \varepsilon_z > 0$, $\varepsilon_y < 0$	$\varepsilon_y, \varepsilon_z > 0$, $\varepsilon_x < 0$	$\varepsilon_x, \varepsilon_y > 0$, $\varepsilon_z < 0$
	760 - 820	1365 - 1610		545 - 850	820 - 972	958 - 1010
Isotope	$hB^{10}N$	$hB^{11}N$	hBN	Nat. Ab.		
	98.7%	99.2%	Nat. Ab.			

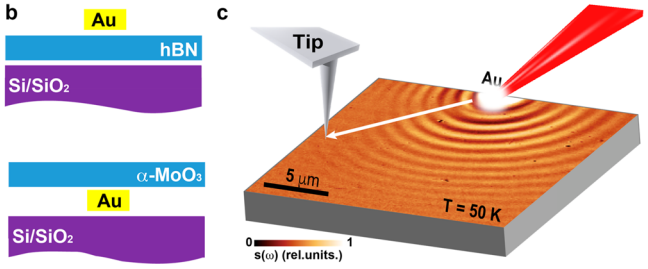

Figure 1. Nano-IR imaging of phonon polaritons in hyperbolic structures at cryogenic temperatures. (a) Table with properties of examined hyperbolic materials. The listed hyperbolic bands are for naturally abundant hBN and α-MoO_3. (b) Sketch of the layered Au/hBN and α-MoO_3/Au structures. The lithographically defined gold (Au) microstructures on top of the hBN (or below the α-MoO_3) serve as effective polaritonic launchers. (c) Nanoscale infrared image of phonon polariton fringes from the Au/$h^{11}BN$, expressed by the normalized scattering amplitude s acquired at a temperature of $T = 50$ K. The arrows represent the propagation direction of the polaritonic waves. These experiments simultaneously visualize the local electric field associated with interference fringe patterns from phonon polaritons launched by the Au microstructures.

We begin with a survey of a large-area (25×20 μm^2) image of HPP standing waves in $h^{11}BN$ obtained at $T = 50$ K (Figure 1c) with an IR laser operating at $\lambda_{IR} = 6.6$ μm. Here we display raw data in the form of the scattered near-field amplitude s normalized to the corresponding signal detected from the gold disks, whose optical response provides a convenient temperature (T)-independent reference. The most prominent aspect of the image in Figure 1c is that the entire field of view is filled with HPP fringes. As expected, the λ_p-fringes dominate the field of view, emanating from the Au antenna and propagating radially outward. Even a cursory inspection of Figure 1c reveals that HPPs remain confined with $\lambda_{IR}/\lambda_p > 5$, and yet, they travel over tens of microns, far exceeding previous measurements at ambient temperature.[6,14]

Nano-IR data in Figure 2 attest to a clear reduction of HPP losses in monoisotopic hBN specimens at lower temperatures with the incident frequency of 1522 cm^{-1} (6.57 μm). HPPs in $h^{11}BN$ films (thickness of 180 nm) at room temperature exhibit 5 μm propagation lengths ($L_p = 1/(2\mathrm{Im}\{q_p\})$, where $q_p = q_p' + iq_p''$, see below), corresponding to quality factor $Q_p \sim 35$ as defined below (Figure 2d,e). As the temperature is reduced, we observe a systematic increase in quality factor and propagation length. Specifically, at $T = 45$ K, Q_p exceeds 60, which represents the highest quality factor achieved to date. To elucidate the underlying polariton scattering mechanisms, we have also performed T-dependent studies in $h^{10}BN$ and naturally abundant samples for systematic comparisons (Figure 2a,c). Two observations can be drawn. First, we observed that the monoisotopic specimens of $h^{10}BN$ and $h^{11}BN$ share nearly identical propagation lengths at all temperatures. These HPP oscillations exhibit scattering lifetimes 2−3 times longer than those observed in naturally abundant hBN crystals, consistent with prior results.[6] Second, HPP propagation lengths at a given frequency generally increase with reduced temperatures for all hBN specimens, as documented in Figure 2d,e. Notably, we found that both $h^{10}BN$ and $h^{11}BN$ exhibit different temperature dependences compared with naturally abundant hBN crystals of similar thickness, as manifested by their HPP oscillations and the quality factor Q_p (Figure 2d,e). These overall trends suggest different underlying mechanisms of phonon scattering between isotopically pure and naturally abundant hBN, as discussed in the following sections in detail.

We have also investigated the temperature dependence of hyperbolic HPP in exfoliated crystals of α-MoO_3, a natural material that exhibits in-plane hyperbolicity at mid-IR frequencies, to determine if the same temperature-dependent scattering is observed as in hBN.[14,15,17] In contrast to the convex wavefronts in isotropic materials, concave wavefronts of the HPP modes in thin slabs of α-MoO_3 have been observed at ambient conditions.[14,15,17,18] In Figure 3, we show raster scans of an α-MoO_3 crystals (~200 nm thickness) exfoliated onto an Au antenna obtained at temperatures ranging from 50 to 300 K and at the frequency of 928 cm^{-1}. At room temperature, HPP interference fringes with concave shapes along the (100) direction were observed, consistent with the isofrequency curves as expected from the in-plane hyperbolic responses.[14,15,17] As the temperature is reduced, we observe a systematic increase in both the overall propagation distance and the number of detectable HPP oscillations, consistent with hBN results. The damping rate in α-MoO_3 is lower across temperatures than in natural hBN, while slightly higher than in monoisotopic hBN. At $T = 50$ K, HPP oscillations approach propagation lengths of 20 μm (Figure 3a). Similar temperature dependence of HPP was also detected in the elliptical response regime (see Supporting Information). These overall trends are similar to our results on hBN isotopes, indicating the uniform characteristics of phonon propagation and dissipation emerging at low temperatures in hyperbolic crystals.

To quantify the dynamics underlying the propagation of HPPs in hBN and α-MoO_3 crystals, we present an analysis based on the complex momentum of the polariton $q_p = q_p' + iq_p''$. The real part defines the wavelength through $\lambda_p = 2\pi/q_p'$, whereas the imaginary part q_p'' quantifies dissipation and the quality factor $Q_p = q_p'/q_p''$. To quantify Q_p, we fit the oscillating line-profiles away from the Au antenna employing the spheroidal model with an analytical formula of $S(x) = \frac{A\sin(q_p' x + B)e^{-q_p'' x}}{\sqrt{x+\zeta}}$, with complex paramters q_p and real A, B, and ζ as fitting parameters[26] (see Supporting Information for details). This analytical formula accounts for fringe decay processes away from the antenna with the presence of a finite damping ($q_p'' > 0$) and a geometric spreading term in the denominator. As shown by solid curves superimposed on polariton line-profiles in Figure 2d and Figure 3b, the fitted results match well with the experimental data across variable temperatures. This analysis allowed us to extract the temperature-dependent quality factors Q_p (T) for polaritons in all isotopes of hBN and α-MoO_3 crystals for the first time, as presented in Figure 2e and Figure 3c. Specifically, we found the highest quality factor Q_p (T) > 60 in near-monoisotopic hBN flakes at cryogenic temperatures.

We now outline the damping rate analysis based on the temperature-dependent results extracted from hBN crystals. In Figure 4, we plot the temperature-dependent HPP damping

https://doi.org/10.1021/acs.nanolett.1c01562
Nano Lett. 2021, 21, 5767−5773

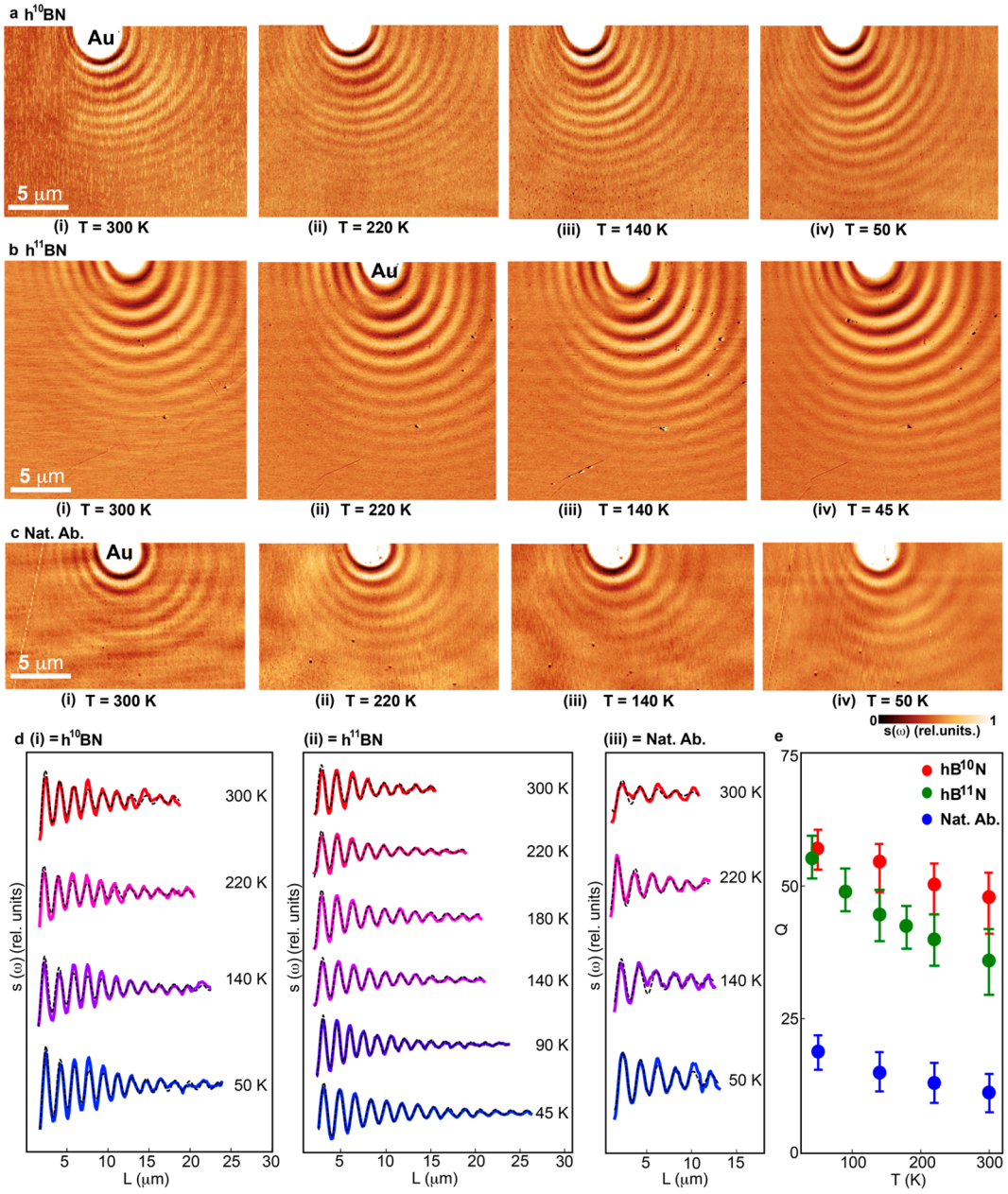

Figure 2. Temperature dependence of phonon polariton propagation in isotopic hBN devices. (a–c) Nano-IR images of the normalized scattering amplitude s acquired at sequential sample temperatures from $h^{10}BN$, $h^{11}BN$, and naturally abundant hBN, respectively. A gold disk (labeled Au) functions as an antenna that launches hBN phonon polariton waves. (d) Line profiles of phonon polariton fringes propagating from left to right, as a function of the distance L from the gold launcher. The variable attenuation of the propagating waveform (solid curves) is characteristic of the temperature-dependent phonon polariton damping rate. Dash-dotted lines are fittings of the wave profile using damped sinusoidal functions corrected by geometric decaying factors (see main text and Supporting Information). (e) The temperature dependence of the quality factor Q_p for phonon polariton waves obtained from nanoscale infrared images shown in panels a–d. The thickness of $h^{10}BN$, $h^{11}BN$, and naturally abundant hBN flakes are 150, 200, and 180 nm, respectively.

rates (line width) $\gamma(T) = \omega v_g/(Q_p(T)v_p)$ converted from quality factors, where v_g and v_p are the group and phase velocities of the modes. Note that the damping rates are on the order of several wavenumbers (approaching $\omega/1000$), while the quality factors defined in terms of momenta are relatively small due to the very low group-phase velocity ratio: $\frac{v_g}{v_p} \sim 0.04$ (obtained from theoretical HPP dispersions, see Supporting Information). Several pieces of information arise from Figure 4. First, the HPP damping rates scale quasi-linearly with temperature for all samples. This is different from the nonlinear temperature dependence of plasmon damping rates observed in pristine graphene.[8] Second, compared to $h^{11}BN$ and $h^{10}BN$, the polariton damping rate in naturally abundant hBN displays a higher residual damping in the zero-Kelvin limit and a steeper slope to the temperature dependence.

The temperature-dependent studies offer insights into the damping mechanisms of HPP in both hBN and α-MoO_3 crystals. We posit that the temperature dependence can only be described by the participation of acoustic phonons in the scattering process, as the optical phonons are not thermally occupied in the temperature range of $T < 300\ K = 208\ cm^{-1}$

https://doi.org/10.1021/acs.nanolett.1c01562
Nano Lett. 2021, 21, 5767–5773

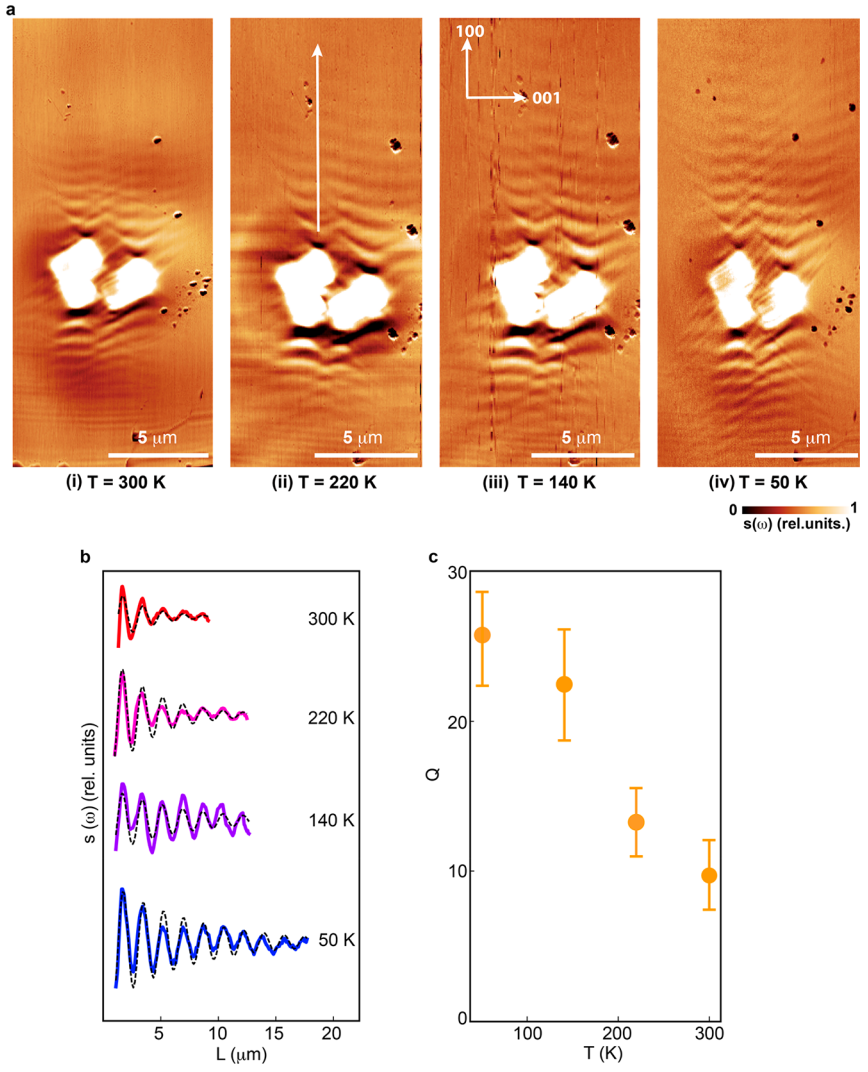

Figure 3. Temperature dependence of phonon polariton propagation in α-MoO_3 crystals. (a) Nano-IR images of the normalized near-field scattering amplitude s acquired at sequential sample temperatures from α-MoO_3 crystals. A pair of gold disks beneath the α-MoO_3 crystal function as antennas that launch polaritonic waves. The white arrow indicates the location of extracted line profiles of phonon polaritons. (b) Line profiles of phonon polariton fringes propagating from left to right, as a function of the distance L from the gold launcher. Dash-dotted lines represent the results of numerical simulations performed to identify the temperature dependence of the complex phonon polariton wavevector and associated damping rate (see main text and Supporting Information). (c) Temperature dependence of the quality factor Q_p of phonon polariton waves obtained from nanoscale infrared images shown in panel a.

(see Supporting Information). In isotopically pure hBN, we attribute the leading damping channel to momentum relaxation caused by acoustic phonons, that is, the polariton being scattered from its initial state with momentum k_i to the final state with momentum $k_f = k_i + q$ by absorbing/emitting an acoustic phonon with momentum $\pm q$ (Figure 4b). Under reasonable approximations (see Supporting Information, section 4.1), the resulting scattering rate reads $\gamma_a(\omega, T) \sim \gamma_{a0}(\omega) f\left(\frac{T}{T_\Lambda}\right)$, where $\gamma_{a0}(\omega)$ is a characteristic scattering rate, $T_\Lambda = v_a\Lambda/k_B$ is a temperature "cutoff", v_a is the speed of acoustic phonons, and Λ is the momentum cutoff of the hyperbolic polaritons. The temperature dependence is captured by the scaling function $f\left(\frac{T}{T_\Lambda}\right)$, which behaves as $1 + \frac{8\pi^4}{15}\left(\frac{T}{T_\Lambda}\right)^4$ when $T \ll T_\Lambda$ and as $1 + \frac{8}{3}\frac{T}{T_\Lambda}$ when $T \gg T_\Lambda$.

Isotopic impurities in natural hBN can also induce the same decay process as acoustic phonons, giving rise to a temperature-independent scattering rate $\gamma_i(\omega)$. Both $\gamma_i(\omega)$ and $\gamma_{a_0}(\omega)$ are proportional to the polariton density of states $D(\omega) = \partial_\omega\sqrt{-\frac{\epsilon_x}{\epsilon_z}}$, where ϵ_x and ϵ_z are the in-plane/out-of-plane dielectric functions of hBN. Here $D(\omega)$ diverges as $\frac{1}{(\omega - \omega_{TO})^{3/2}}$ when the frequency approaches the transverse optical (TO) phonon, while weakly depending on $\frac{1}{(\omega_{LO} - \omega)^{1/2}}$ as the frequency approaches the longitudinal optical (LO) phonons. Such a strong frequency dependence suggests that the frequency-dependent damping rate $\gamma(\omega)$ needs to replace its constant counterpart in the Lorentzian oscillator model. Note that polaritons with frequency ω can also decay into E_{1u} TO phonons or E_{2g} phonons (nearly flat dispersion at the frequency $\omega_{TO} = \omega_g = 1360$ cm^{-1}) by emitting an acoustic phonon. This contributes to a scattering rate $\gamma_g(\omega,T)$ =

https://doi.org/10.1021/acs.nanolett.1c01562
Nano Lett. 2021, 21, 5767−5773

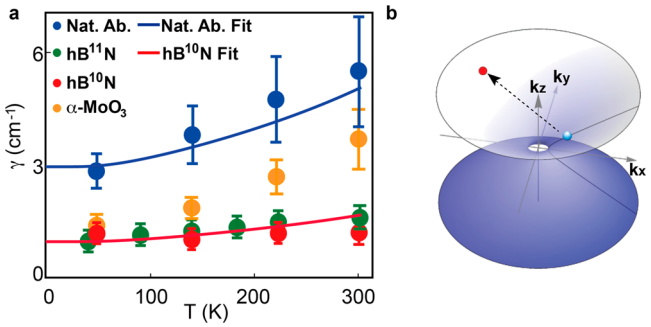

Figure 4. Theoretical modeling of phonon polariton damping rate γ in hyperbolic crystals. (a) The dots corresponding to the extracted dissipation factors as a function of temperature; the solid blue and red lines are the theoretical fitting results as detailed in the main text. The parameters used here are $hB^{11}N$: ω = 1522 cm^{-1}, v_g/v_p = 0.037; $hB^{10}N$: ω = 1553 cm^{-1}, v_g/v_p = 0.039; naturally abundant hBN: ω = 1522 cm^{-1}, v_g/v_p = 0.039; B^{11}: α-MoO_3 = 928 cm^{-1}, v_g/v_p = 0.039. The group and phase velocity in α-MoO_3 are taken from ref 14. (b) The illustration of scattering of a hyperbolic polariton from an initial state (blue dot) to a final state (red dot) on the iso-frequency surface by either emitting/obsorbing an acoustic phonon or by impurity potential.

$\gamma_{g_0}(\omega)(n_b(\omega - \omega_{TO}) + 1)$ where the boson occupation number n_b gives the temperature dependence and γ_{g_0} is a frequency scale depending on ω. However, our theoretical modeling suggests that this term is negligibly small (see Supporting Information, section 4). The functional forms of γ_a, γ_i, and γ_g, therefore, represent these new results.

The steeper temperature-dependence of damping rate in natural hBN implies a higher-order decay channel involving both impurities and acoustic phonons, which we subsume by $\gamma_h(T) = \kappa_i(\omega)(\gamma_a(\omega,T) + \gamma_g(\omega,T))$ (see Supporting Information). The total polariton damping rates for natural and isotopically pure hBN are thus

$$\gamma_{iso}(T) = \gamma_0 + \gamma_a(T) + \gamma_g(T) \text{ and } \gamma_{nat}(T) = \gamma_{iso}(T) + \gamma_i + \gamma_h(T)$$

where γ_0 is a temperature-independent scattering rate due to other decay processes.[28,29] The dashed fitting lines in Figure 4 correspond to γ_0 = 0.4 cm^{-1}, γ_{a_0} = 0.6 cm^{-1}, γ_{g_0} = 0, γ_i = 0.5 cm^{-1}, κ_i = 2.5, and T_Λ = 450 K. Note that these fitting parameters are obtained for our simplified analytical model. Further dedicated first-principle calculations are possibly needed for fine-tuning, which is beyond the scope of the current work. On top of the above intrinsic damping channels, the dielectric loss from the SiO_2 substrate contributes <20% to the total damping rate at the experimental frequency of 1522 cm^{-1}.

In summary, our results account for HPP dynamics in high-quality hyperbolic crystals. Quality factors and scattering rates of hyperbolic polaritons in naturally abundant and monoisotopic hBN, as well as α-MoO_3, have been extracted from cryogenic nanoimaging studies. Though limited by acoustic phonon scattering and other decay channels, the HPP propagation length and lifetime in monoisotopic hBN at low-T exceed 8 μm and 5 ps, a new record among all-natural hyperbolic materials reported so far. Our first report of HPP nanoimaging studies of high-quality hyperbolic crystals at cryogenic temperatures demonstrates promising opportunities for the exploration of advanced phononic switching,[30] polariton periodic orbits in cavities,[31] and nonlinear phenomena[32] in ultrapure polar samples at technologically relevant liquid nitrogen temperatures. Long-lived polaritons are of interest for applications in infrared signal processing, nanophotonic circuits, nanolight sensing and communications, as well as heat management at the nanoscale.[14,18]

Methods. *1. Sample Growth and Device Fabrication.* hBN crystals with the natural distribution of isotopes (20% B-10 and 80% B-11) were produced using a hot-pressed boron nitride ceramic boat, which served as both the container for the metal flux and as the B and N sources. For B^{10} and B^{11}-enriched hBN crystal growth, the procedure is modified to use elemental boron as a source material. Therefore, the boron nitride boat was replaced with an alumina crucible. High-purity 10B (99.22%) or 11B (99.41%) powders were mixed with Ni and Cr powders to give overall concentrations of 4% B, 48% Ni and 48% Cr. In this case, all nitrogen in the hBN originated from the flowing N_2 gas. Other than these changes, the procedure was the same as described above. The hBN crystals were then transferred onto SiO_2/Si substrates using the mechanical exfoliation method. After identifying the crystal thickness and uniformity, standard E-beam lithography is utilized to define Au launchers, followed by thermal annealing processes to remove contaminated polymer residuals.

2. Cryogenic IR Nanoimaging Experiments. IR nanoimaging experiments were performed using a home-built scattering-type scanning near-field optical microscope (s-SNOM) operating with variable sample temperatures from 50−300 K. All measurements are conducted under ultrahigh vacuum conditions at pressured $<10^{-9}$ mbar to prevent sample surface contamination. The cryogenic s-SNOM is equipped with continuous-wave mid-IR quantum cascade lasers (daylightsolutions.com) and CO_2 lasers (accesslaser.com). The s-SNOM is based on an atomic force microscope (AFM), operated for the present experiments in noncontact mode using cantilevered metallic AFM probes with tip apex radius ~25 nm and tapping frequencies ~270 kHz. A pseudoheterodyne interferometric detection module is implemented in our s-SNOM to extract both scattering amplitude s and phase of the near-field signal. In the current work, we discuss only the former. In order to suppress background contributions to the backscattered near-field signal, we demodulated the detected signal at the third harmonic of the probe tapping frequency.

■ ASSOCIATED CONTENT

Supporting Information

The Supporting Information is available free of charge at https://pubs.acs.org/doi/10.1021/acs.nanolett.1c01562.

Detailed description of the device fabrication and characterization, spheroidal modeling of the near field signal, dispersion of hyperbolic phonon polaritons, and discussion of the phonon polariton damping rate (PDF)

■ AUTHOR INFORMATION

Corresponding Authors

Guangxin Ni − *Department of Physics, Florida State University, Tallahassee, Florida 32306, United States; National High Magnetic Field Laboratory, Florida State University, Tallahassee, Florida 32310, United States;* orcid.org/0000-0002-7216-1829; Email: guangxin.ni@magnet.fsu.edu

https://doi.org/10.1021/acs.nanolett.1c01562
Nano Lett. 2021, 21, 5767−5773

D. N. Basov − *Department of Physics, Columbia University, New York 10027, United States*; Email: db3056@columbia.edu

Authors

Alexander S. McLeod − *Department of Physics, Columbia University, New York 10027, United States*
Zhiyuan Sun − *Department of Physics, Columbia University, New York 10027, United States*
Joseph R. Matson − *Department of Mechanical Engineering, Vanderbilt University, Nashville, Tennessee 37235, United States*
Chiu Fan Bowen Lo − *Department of Physics, Columbia University, New York 10027, United States*
Daniel A. Rhodes − *Department of Mechanical Engineering, Columbia University, New York 10027, United States;* orcid.org/0000-0002-7651-3211
Francesco L. Ruta − *Department of Physics and Department of Applied Physics and Applied Mathematics, Columbia University, New York 10027, United States;* orcid.org/0000-0002-8746-9420
Samuel L. Moore − *Department of Physics, Columbia University, New York 10027, United States*
Rocco A. Vitalone − *Department of Physics, Columbia University, New York 10027, United States*
Ramon Cusco − *Lluís Solé i Sabarís s.n., GEO3BCN-CSIC, 08028 Barcelona, Spain;* orcid.org/0000-0001-9490-4884
Luis Artús − *Lluís Solé i Sabarís s.n., GEO3BCN-CSIC, 08028 Barcelona, Spain*
Lin Xiong − *Department of Physics, Columbia University, New York 10027, United States*
Cory R. Dean − *Department of Physics, Columbia University, New York 10027, United States*
James C. Hone − *Department of Mechanical Engineering, Columbia University, New York 10027, United States*
Andrew J. Millis − *Department of Physics, Columbia University, New York 10027, United States*
Michael M. Fogler − *Department of Physics, University of California, San Diego, La Jolla, California 92093, United States*
James H. Edgar − *Tim Taylor Department of Chemical Engineering, Kansas State University, Manhattan, Kansas 66506, United States;* orcid.org/0000-0003-0918-5964
Joshua D. Caldwell − *Department of Mechanical Engineering, Vanderbilt University, Nashville, Tennessee 37235, United States;* orcid.org/0000-0003-0374-2168

Complete contact information is available at: https://pubs.acs.org/10.1021/acs.nanolett.1c01562

Author Contributions

All authors were involved in designing the research, performing the research, and writing the paper.

Notes

The authors declare no competing financial interest.

■ ACKNOWLEDGMENTS

Research at Columbia is supported by Vannevar Bush Faculty Fellowship ONR-VB: N00014-19-1-2630. We thank A. Sternbach and S. Zhang for helpful discussions. Exfoliation and transfer of hBN onto desired substrates and electron beam lithography of gold disks were performed by J.T.M. and supported by the National Science Foundation (DMR1904793). Additional structure fabrication was supported by the Center on Precision-Assembled Quantum Materials, funded through the U.S. National Science Foundation (NSF) Materials Research Science and Engineering Centers (award no. DMR-2011738). Initial simulations and experimental design from Vanderbilt were provided by J.D.C. in collaboration with the Columbia team (D.N.B. and G.N.) and was supported by the Office of Naval Research (N00014-18-1-2107). The hBN phonon band structure calculation was performed by R.C. and L.A. and supported by the Spanish MINECO/FEDER grant (MAT2015-71035-R). Cryogenics nano-optics experiments at Columbia were solely supported as part of Programmable Quantum Materials, an Energy Frontier Research Center funded by the U.S. Department of Energy (DOE), Office of Science, Basic Energy Sciences (BES), under award no. DE-SC0019443. D.N.B is the Gordon and Betty Moore Foundation's EPiQS Initiative Investigator no. 9455.

■ REFERENCES

(1) Basov, D. N.; Fogler, M. M.; Garcia de Abajo, F. J. Polaritons in van der Waals materials. *Science* **2016**, *354*, aag1992.
(2) Low, T.; et al. Polaritons in layered two-dimensional materials. *Nat. Mater.* **2017**, *16*, 182−194.
(3) Caldwell, J. D.; Lindsay, L.; Giannini, V.; Vurgaftman, I.; Reinecke, T. L.; Maier, S. A.; Glembocki, O. J.; et al. Low-loss, infrared and terahertz nanophotonics using surface phonon polaritons. *Nanophotonics* **2015**, *4*, 44.
(4) Dai, S.; et al. Tunable phonon polaritons in atomically thin van der Waals crystals of boron nitride. *Science* **2014**, *343*, 1125−1129.
(5) Li, P.; Lewin, M.; Kretinin, A. V.; Caldwell, J. D.; Novoselov, K. S.; Taniguchi, T.; Watanabe, K.; Gaussmann, F.; Taubner, T. Hyperbolic phonon-polaritons in boron nitride for near-field optical imaging and focusing. *Nat. Commun.* **2015**, *6*, 1−9.
(6) Giles, A. J.; et al. Ultralow-loss polaritons in isotopically pure boron nitride. *Nat. Mater.* **2018**, *17*, 134−139.
(7) Basov, D. N.; Asenjo-Garcia, A.; Schuck, P. J.; Zhu, X. Y.; Rubio, A. Polaritons Panorama. *Nanophotonics* **2020**, *10*, 549.
(8) Ni, G. X.; et al. Fundamental limits to graphene plasmonics. *Nature* **2018**, *557*, 530−533.
(9) Jiang, B.-Y.; Ni, G.-X.; Addison, Z.; Shi, J. K.; Liu, X.; Zhao, S. Y. F.; Kim, P.; Mele, E. J.; Basov, D. N.; Fogler, M. M. Plasmon reflections by topological electronic boundaries in bilayer graphene. *Nano Lett.* **2017**, *17*, 7080−7085.
(10) Ni, G. X.; et al. Plasmons in graphene moiré superlattices. *Nat. Mater.* **2015**, *14*, 1217−1222.
(11) Goldflam, M. D.; Ni, G.-X.; Post, K. W.; Fei, Z.; Yeo, Y.; Tan, J. Y.; Rodin, A. S.; Chapler, B. C.; Ozyilmaz, B.; Castro Neto, A. H.; Fogler, M. M.; Basov, D. N. Tuning and persistent switching of graphene plasmons on a ferroelectric substrate. *Nano Lett.* **2015**, *15*, 4859−4864.
(12) Sunku, S. S.; et al. Photonic crystals for nano-light in moire graphene superlattices. *Science* **2018**, *362*, 1153−1156.
(13) Fei, Z.; Ni, G.-X.; Jiang, B.-Y.; Fogler, M. M.; Basov, D. N. Nanoplasmonics phenomena at electronic boundaries in graphene. *ACS Photonics* **2017**, *4*, 2971−2977.
(14) Ma, W.; et al. In-plane anisotropic and ultra-low-loss polaritons in a natural van der Waals crystal. *Nature* **2018**, *562*, 557−562.
(15) Zheng, Z.; et al. A mid-infrared biaxial hyperbolic van der Waals crystal. *Science Adv.* **2019**, *5*, eaav8690.
(16) Hu, G.; et al. Topological polaritons and photonic magic angles in twisted α-MoO_3 bilayers. *Nature* **2020**, *582*, 209−213.
(17) Zheng, Z.; Chen, J.; Wang, Y.; Wang, X.; Chen, X.; Liu, P.; Xu, J.; Xie, W.; Chen, H.; Deng, S.; Xu, N. Highly confined and tunable hyperbolic phonon polaritons in van der Waals semiconducting transition metal oxides. *Adv. Mater.* **2018**, *30*, 1705318.

(18) Chen, M.; et al. Configurable phonon polaritons in twisted α-MoO_3. *Nat. Mater.* **2020**, *19*, 1307−1311.
(19) Duan, J.; et al. Twisted nano-optics: manipulating light at the nanoscale with twisted phonon polariton slabs. *Nano Lett.* **2020**, *20*, 5323−5329.
(20) McLeod, A. S.; et al. Nanotextured phase coexistence in the correlated insulator V_2O_3. *Nat. Phys.* **2017**, *13*, 80−86.
(21) McLeod, A. S.; et al. Multi-messenger nanoprobes of hidden magnetism in a strained magnanite. *Nat. Mater.* **2020**, *19*, 397−404.
(22) Post, K. W.; et al. Coexisting first- and second-order electronic phase transitions in a correlated oxide. *Nat. Phys.* **2018**, *14*, 1056−1061.
(23) Ni, G. X.; et al. Ultrafast optical switching of infrared plasmon polaritons in high-mobility graphene. *Nat. Photonics* **2016**, *10*, 244−247.
(24) Ni, G. X.; Wang, H.; Jiang, B.-Y.; Chen, L. X.; Du, Y.; Sun, Z. Y.; Goldflam, M. D.; Frenzel, A. J.; Xie, X. M.; Fogler, M. M.; Basov, D. N.; et al. Soliton superlattices in twisted hexagonal boron nitride. *Nat. Commun.* **2019**, *10*, 1−6.
(25) Berkowitz, M. E.; et al. Hyperbolic cooper-pair polaritons in planar graphene/cuprate plasmonic cavities. *Nano Lett.* **2021**, *21*, 308−316.
(26) Tamagnone, M.; Ambrosio, A.; Chaudhary, K.; Jauregui, L. A.; Kim, P.; Wilson, W. L.; Capasso, F. Ultra-confined mid-infrared resonant phonon polaritons in van der Waals nanostructures. *Science Adv.* **2018**, *4*, eaat7189.
(27) Fali, A.; et al. Refractive index-based control of hyperbolic phonon polariton propagation. *Nano Lett.* **2019**, *19*, 7725−7734.
(28) Segura, A.; Cuscó, R.; Taniguchi, T.; Watanabe, K.; Artús, L. Long lifetime of the E1u in-plane infrared-active modes of h-BN. *Phys. Rev. B: Condens. Matter Mater. Phys.* **2020**, *101*, 235203.
(29) Cuscó, R.; Gil, B.; Cassabois, G.; Artús, L. Temperature dependence of Raman-active phonons and anharmonic interactions in layered hexagonal BN. *Phys. Rev. B: Condens. Matter Mater. Phys.* **2016**, *94*, 155435.
(30) Stupakiewicz, A. Ultrafast phononic switching of magnetization. *Nat. Phys.* **2021**, *17*, 489.
(31) Sun, Z.; Gutierrez-Rubio, A.; Basov, D. N.; Fogler, M. M. Hamiltonian optics of hyperbolic polaritons in nanogranules. *Nano Lett.* **2015**, *15*, 4455−4460.
(32) Gu, M.; Rondinelli, M. Nonlinear phonic control and emergent magnetism in Mott insulating titanates. *Phys. Rev. B: Condens. Matter Mater. Phys.* **2018**, *98*, 024102.

https://doi.org/10.1021/acs.nanolett.1c01562
Nano Lett. 2021, 21, 5767−5773

Supplementary Information

Long-lived phonon polaritons in hyperbolic materials

Guangxin Ni[1,2,*], Alexander S. McLeod[3], Zhiyuan Sun[3], Joseph R. Matson[4], Chiu Fan Bowen Lo[3], Daniel A. Rhodes[5], Francesco L. Ruta[3,6], Samuel L. Moore[3], Rocco A. Vitalone[3], Ramon Cusco[7], Luis Artús[7], Lin Xiong[3], Cory R. Dean[3], James C. Hone[5], Andrew J. Millis[3], Michael M. Fogler[8], James H. Edgar[9], Joshua D. Caldwell[4], D. N. Basov[3,*]

[1]Department of Physics, Florida State University, Tallahassee, Florida 32306, USA.
[2]National High Magnetic Field Laboratory, Tallahassee, Florida 32310, USA.
[3]Department of Physics, Columbia University, New York, NY 10027, USA.
[4]Department of Mechanical Engineering, Vanderbilt University, Nashville, Tennessee 37235, USA.
[5]Department of Mechanical Engineering, Columbia University, New York, NY 10027, USA.
[6]Department of Applied Physics and Applied Mathematics, Columbia University, New York, NY 10027, USA.
[7]GEO3BCN-CSIC, Lluís Solé i Sabarís s.n., 08028 Barcelona, Spain.
[8]Department of Physics, University of California, San Diego, La Jolla, California 92093, USA.
[9]Tim Taylor Department of Chemical Engineering, Kansas State University, Manhattan, KS 66506, USA.
*Corresponding author: guangxin.ni@magnet.fsu.edu, db3056@columbia.edu.

1. Device fabrication and characterization

All of our naturally abundant hexagonal boron nitride (hBN), isotopic hBN and α-MoO_3 micro-crystals were obtained using mechanical exfoliation. For both of the naturally abundant hBN and isotopic hBN samples, standard E-beam lithography were carried out to pattern Au micro-disks on top of a pre-examined hBN flakes followed by thermal annealing to remove polymer residues on top of the hBN surface (Fig. S1a). In contrast, for α-MoO_3 samples, substrate with pre-patterned Au microstructures were utilized during the exfoliation steps (Fig. S2a). The typical AFM topography image of the hBN and α-MoO_3 devices are shown in Fig. S1b and Fig. S2a. Figures S1c and Fig. 2b-e show the corresponding near-field image of hBN and α-MoO_3 at variable incident light excitations and temperatures. Clear phonon polariton fringes along the Au antenna can be detected, which are discussed in the main text and also Fig. S1&S2 shown below.

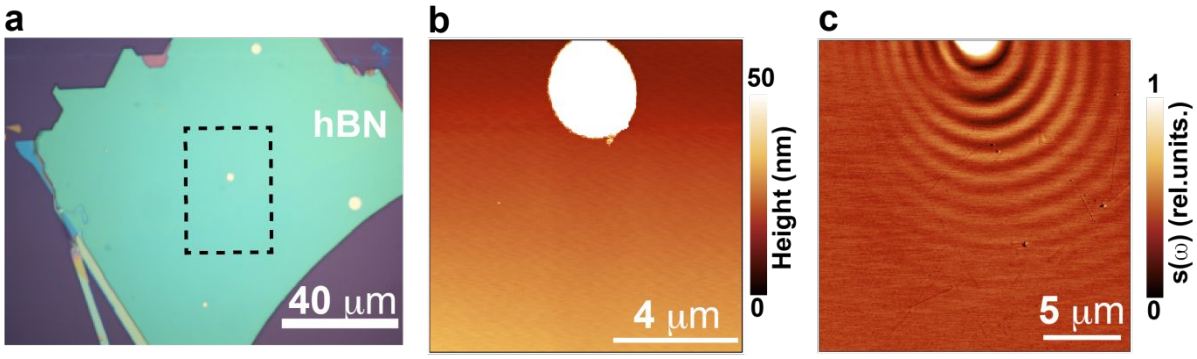

Figure S1 | AFM topography and $s(\omega)$ image of the isotopic hBN device. a, Optical imaging of the hBN sample under study. The black dashed indicates the regime of interests for the subsequent nano-IR imaging. b & c, AFM topography and $s(\omega)$ image of the isotopic hBN device.

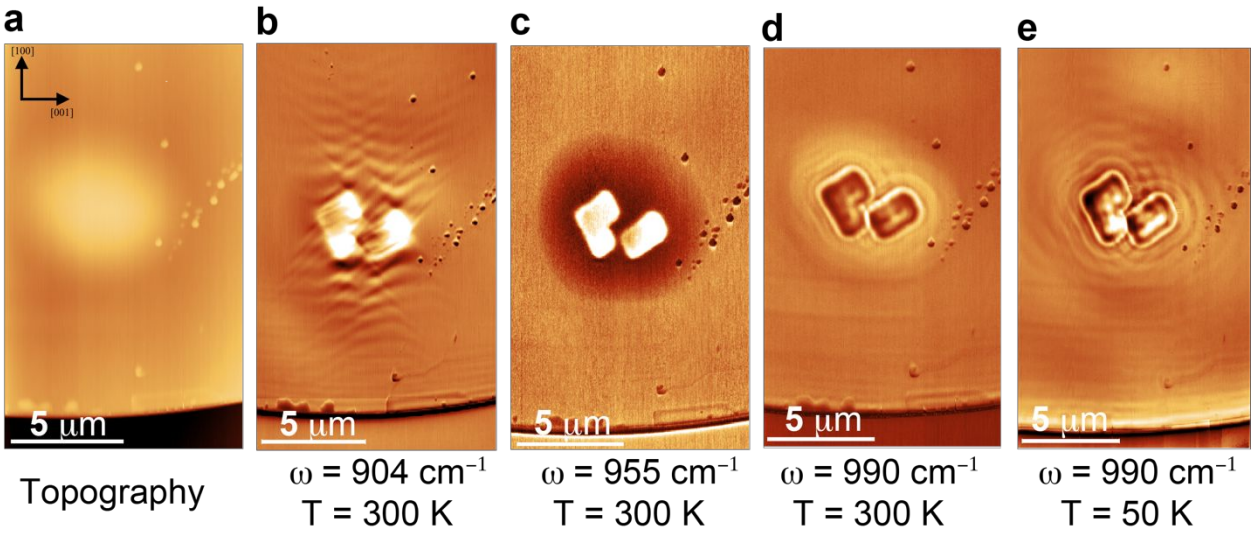

Figure S2 | AFM topography and $s(\omega)$ image of the α-MoO_3 device. a, Topography imaging of the α-MoO_3 sample under study. The pre-patterned Au microstructures are underneath the α-MoO_3 flake. **b-e**, $s(\omega)$ image of the α-MoO_3 device at various frequencies and temperatures.

2. Spheroidal modeling of the near field signal

To model the s-SNOM images and quantify the propagation damping rate quantitatively, we used the spheroidal model as described previously [1-4]. From this model, we are going to prove the simplified near field fringe profile: $S(x) \sim \frac{\sin(q'x + \phi)}{\sqrt{x}} e^{-q''x}$.

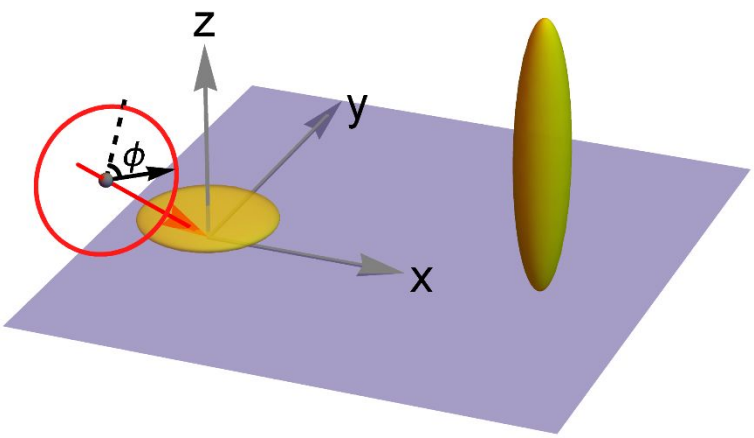

Figure S3, Spheroidal model of the launcher and the tip. Launcher is an oblate spheroid and tip is a prolate one, with symmetric axis along z. Both are assumed to be perfect metals and the system is small enough compared to the vacuum wavelength λ_0 of incident photons. The incident plane is $y-z$ plane and the incident angle is θ_{in}. The polarization angle is ϕ with $\phi = 0$ meaning p-wave and $\phi = \pi/2$ meaning s-wave.

The modeling is depicted in Fig. S3. The gold launcher and tip are treated as spheroids made of perfect metal, whose centers are located at $(0,0,z_g)$ and $(x_t,0,z_t)$. Although the gold launcher is actually a rectangle, the strongest plasmonic emission still comes from its three (x,y,z direction) most dipolar active surface modes, which is reasonably captured by the three dipolar modes of the oblate spheroid. The near field signal is simply the total electrical dipole moment of the whole system which we compute in the following.

The prelate spheroidal coordinate system (η,θ,ϕ) is defined by the transformation with the Cartesian coordinate:

$$x = a\sinh(\eta)\sin(\theta)\cos(\phi),\ y = a\sinh(\eta)\sin(\theta)\sin(\phi),\ z = a\cosh(\eta)\cos(\theta). \quad \text{(S12)}$$

The tip surface is described by the constant η surface $\eta = \eta_0$. The electric field potential outside of the tip satisfies $\nabla^2\Phi = 0$ and can be decomposed into

$$\Phi^t_{in} = \sum_{lm} A^t_{lm} P^m_l(\cosh\eta) Y^m_l(\theta,\phi),\ \ \Phi^t_{out} = \sum_{lm} B^t_{lm} Q^m_l(\cosh\eta) Y^m_l(\theta,\phi) \quad \text{(S13)}$$

where P^m_l/Q^m_l are associated Legendre functions of the first/second kind and $Y^m_l(\theta,\phi) = P^m_l(\cos\theta)e^{im\phi}$ are spheroidal harmonics. Φ_{in} are non-evanescent 'incident' potentials while Φ_{out} are outgoing potentials since they are evanescent. Only the $l = 1$ modes have nonzero dipole moments that can be directly excited and radiate into far field which we focus on. It is more convenient to use the xyz basis for the three $l = 1$ modes

$$\left(\Phi^t_{outx},\Phi^t_{outy},\Phi^t_{outz}\right) = \left(Q^1_1(\cosh\eta)\sin\theta\cos\phi,\ Q^1_1(\cosh\eta)\sin\theta\sin\phi,\ Q^0_1(\cosh\eta)\cos\theta\right)$$

$$\left(\Phi^t_{inx},\Phi^t_{iny},\Phi^t_{inz}\right) = (\sinh\eta\sin\theta\cos\phi,\sinh\eta\sin\theta\sin\phi,\cosh\eta\cos\theta) \quad \text{(S14)}$$

since they correspond to dipole moments in the xyz directions. The incident field and response field on a spheroid is decomposed as

$$\Phi_{in}^{t} = A_x^t \Phi_{inx}^t + A_y^t \Phi_{iny}^t + A_z^t \Phi_{inz}^t,$$

$$\Phi_{out}^{t} = B_x^t \Phi_{outx}^t + B_y^t \Phi_{outy}^t + B_z^t \Phi_{outz}^t . \quad \text{(S15)}$$

A uniform incident electric field $\Phi = -\mathbf{E}\cdot\mathbf{r}$ can thus be represented as

$$\mathbf{A}^{\mathrm{t}} = -a\mathbf{E}.$$

Matching the boundary condition $\Phi_{in}^t + \Phi_{out}^t = 0$ on the surface of the spheroid renders $\mathbf{B}^{\mathrm{t}} = \hat{R}_t \mathbf{A}^{\mathrm{t}}$ where

$$\hat{R}_t = -\operatorname{diag}\left(\frac{\sinh\eta_0}{Q_1^1(\cosh\eta_0)}, \frac{\sinh\eta_0}{Q_1^1(\cosh\eta_0)}, \frac{\cosh\eta_0}{Q_1^0(\cosh\eta_0)}\right) \quad \text{(S16)}$$

is the 'reflection coefficient' of the spheroid.

The oblate spheroidal coordinate system (ζ,ξ,ϕ) is defined by

$$x = a\cosh(\zeta)\cos(\xi)\cos(\phi),\ y = a\cosh(\zeta)\cos(\xi)\sin(\phi),\ z = a\sinh(\zeta)\sin(\xi). \quad \text{(S17)}$$

The gold surface is described by the constant ζ surface $\zeta = \zeta_0$. The electric field potential outside of the gold satisfies $\nabla^2\Phi = 0$ and can be decomposed into

$$\Phi_{in}^{g} = \sum_{lm} A_{lm}^g P_l^m(i\sinh\zeta) Y_l^m(\xi,\phi),\ \Phi_{out}^{g} = \sum_{lm} B_{lm}^g Q_l^m(i\sinh\zeta) Y_l^m(\xi,\phi) \quad \text{(S18)}$$

Where the spheroidal harmonics are now changed to $Y_l^m(\xi,\phi) = P_l^m(\sin\xi)e^{im\phi}$. The three $l = 1$ modes are

$$\left(\Phi_{outx}^g, \Phi_{outy}^g, \Phi_{outz}^g\right) = \left(Q_1^1(i\sinh\zeta)\cos\xi\cos\phi,\ Q_1^1(i\sinh\zeta)\cos\xi\sin\phi,\ Q_1^0(i\sinh\zeta)\sin\xi\right)$$

$$\left(\Phi_{inx}^g, \Phi_{iny}^g, \Phi_{inz}^g\right) = (\cosh(\zeta)\cos(\xi)\cos\phi, \cosh(\zeta)\cos(\xi)\sin\phi, \sinh(\zeta)\sin(\xi)) \quad \text{(S19)}$$

The incident field and response field on a spheroid is decomposed as

$$\Phi_{in}^{g} = A_x^g \Phi_{inx}^g + A_y^g \Phi_{iny}^g + A_z^g \Phi_{inz}^g,$$

$$\Phi_{out}^{g} = B_x^g \Phi_{outx}^g + B_y^g \Phi_{outy}^g + B_z^g \Phi_{outz}^g . \quad \text{(S20)}$$

A uniform incident electric field $\Phi = -\mathbf{E}\cdot\mathbf{r}$ can thus be represented as

$$\mathbf{A} = -a\mathbf{E}.$$

The relation $\mathbf{B}^g = \hat{R}_{\mathrm{g}}\mathbf{A}^g$ is similar where

$$\hat{R}_g = -\operatorname{diag}\left(\frac{\cosh(\zeta_0)}{Q_1^1(i\sinh\zeta_0)}, \frac{\cosh(\zeta_0)}{Q_1^1(i\sinh\zeta_0)}, \frac{\sinh(\zeta_0)}{Q_1^0(i\sinh\zeta_0)}\right) \quad \text{(S21)}$$

is the 'reflection coefficient' of the oblate spheroid.

The response field Φ_{out}^g on the gold then perturbs the 2D sample which is modeled as an infinite plane. Afterwards, Φ_{out}^g gets reflected by the sample and the reflected field then polarizes the other

spheroid (the gold disk). This process can be analyzed by decomposing the incident field on the 2D plane, $\Phi_{out}^{g}(x,y,z=0)$, into Fourier components:

$$\Phi_{out}^{g}(x,y)=\sum_{\boldsymbol{q}}\left(B_x^g f_{g1}(q)\cos\theta_{\boldsymbol{q}}+B_y^g f_{g1}(q)\sin\theta_{\boldsymbol{q}}+B_z^g f_{g3}(q)\right)e^{i\boldsymbol{qr}} \text{(S22)}$$

Where

$$f_{g1}(q)=\int dxdy e^{-iqx}\frac{Q_1^1(i\sinh\zeta(x,y))}{\cosh(\zeta(x,y))}(x+iy)=2\pi i\int_0^\infty drr^2\frac{Q_1^1(i\sinh\zeta(r))}{\cosh(\zeta(r))}J_1(-qr) \text{ (S23)}$$

and

$$f_{g3}(q)=\int dxdy e^{-iqx}\frac{Q_1^0(i\sinh\zeta(x,y))}{\sinh(\zeta(x,y))}(0-z_g)=-2\pi z_g\int_0^\infty drr\frac{Q_1^0(i\sinh\zeta(r))}{\sinh(\zeta(r))}J_0(-qr). \text{ (S24)}$$

Each momentum component is reflected by the 2D plane with the reflection coefficient $R_p(\omega,q)$. This reflected field in turn acts as the incident field for the tip:

$$\boldsymbol{A}^t=\hat{G}\boldsymbol{B}^g \text{ (S24)}$$

where

$$G_{ij}=\sum_q\Phi_{outj}^g(\boldsymbol{q})\Phi_{outi}^t(\boldsymbol{q})R_p(\omega,\boldsymbol{q})e^{iq_x x_t} \text{ (S26)}$$

contains the information of tip launched plasmons. Note that we have defined similar Fourier's components of the dipolar modes of the tip:

$$\Phi_{out}^t(q)=\left(f_{t1}(q)\cos\theta_{\boldsymbol{q}},f_{t1}(q)\sin\theta_{\boldsymbol{q}},f_{t3}(q)\right) \text{ (S27)}$$

where

$$f_{t1}(q)=\int dxdy e^{-iqx}\frac{Q_1^1(\cosh\eta(x,y))}{\sinh(\eta(x,y))}(x+iy)=2\pi i\int_0^\infty drr^2\frac{Q_1^1(\cosh\eta(r))}{\sinh(\eta(r))}J_1(-qr) \text{ (S25)}$$

and

$$f_{t3}(q)=\int dxdy e^{-iqx}\frac{Q_1^0(\cosh\eta(x,y))}{\cosh(\eta(x,y))}(0-z_t)=-2\pi z_t\int_0^\infty drr\frac{Q_1^0(\cosh\eta(r))}{\cosh(\eta(r))}J_0(-qr). \text{ (S28)}$$

The incident field then induces a dipole on the tip:

$$\boldsymbol{P}_t=\hat{R}_t\hat{G}\hat{R}_g\boldsymbol{E}=\hat{M}\boldsymbol{E} \quad \text{(S29)}$$

The resulting dipole moment on the tip then radiates into far field which contribute to the signal. Similarly, the tip launched plasmon induces a dipole on the gold:

$$\boldsymbol{P}_g=\hat{R}_g\hat{G}^{\boldsymbol{T}}\hat{R}_t\boldsymbol{E}=\hat{M}^T\boldsymbol{E}. \text{ (S30)}$$

Detailed calculation gives the propagator as

$$\begin{pmatrix} \int dq\, f_{g1}(q) f_{t1}(q) q\, g(q) \left(\frac{J_1(x_0 q)}{x_0 q} - J_2(x_0 q) \right) & 0 & i \int dq\, f_{g1}(q) f_{t3}(q) q\, g(q) J_1(x_0 q) \\ 0 & \int dq\, f_{g1}(q) f_{t1}(q) q\, g(q) \frac{J_1(x_0 q)}{x_0 q} & 0 \\ i \int dq\, f_{g3}(q) f_{t1}(q)\, g(q) J_1(x_0 q) & 0 & \int dq\, f_{g3}(q) f_{t3}(q) q\, g(q) J_0(x_0 q) \end{pmatrix} \quad \text{(S31)}$$

where the integral over q is $\int_0^\infty dq$, $g(q) = \frac{1}{1 - q/q_p V(q)}$ is the plasmonic propagator on the plane and J_n are Bessel functions. The vanishing of G_{i2} is due to the mirror symmetry with respect to $x-z$ plane. Since the imaginary part of $g(q)$ is roughly a delta function peak at $q = q_p$, the imaginary part of $\hat{G}$ is simply

$$\mathrm{Im}[\hat{G}^T] = q_p^3 \begin{pmatrix} f_{g1}(q_p) f_{t1}(q_p) \left(\frac{J_1(x_0 q_p)}{x_0 q_p} - J_2(x_0 q_p) \right) & 0 & i f_{g1}(q_p) f_{t3}(q_p) J_1(x_0 q_p) \\ 0 & f_{g1}(q_p) f_{t1}(q_p) \frac{J_1(x_0 q_p)}{x_0 q_p} & 0 \\ i f_{g3}(q_p) f_{t1}(q_p) J_1(x_0 q_p) & 0 & f_{g3}(q_p) f_{t3}(q_p) J_0(x_0 q_p) \end{pmatrix} \quad \text{(S32)}$$

Due to the fact that the launcher is mostly polarizable along the plane while the tip is mostly polarizable along z, the G_{xz} component will be the dominant contribution to the signal. Therefore, the spatial profile is $S(x) \sim J_1(q_p x) \sim \frac{\sin(q_p x + \phi)}{\sqrt{x}}$. The damping naturally enters as an exponential factor, rendering $S(x) \sim \frac{\sin(q' x + \phi)}{\sqrt{x}} e^{-q'' x}$.

3. Dispersion of hyperbolic phonon polaritons

In this section, we provide the detailed analysis of phonon polariton dispersion in hBN slabs which enables us to convert the quality factors defined in spatial decay to damping rates in time domain. The phonon polariton can be found as the poles of the near field reflection coefficient:

$$R_{slab}(\omega, q) = \frac{R_{12} + e^{2ik_z d} R_{23}}{1 + e^{2ik_z d} R_{12} R_{23}}$$

of an hBN slab where

$$R_{12}(\omega, q) = \frac{1 - \sqrt{\epsilon_x \epsilon_z}}{1 + \sqrt{\epsilon_x \epsilon_z}}, \qquad R_{23}(\omega, q) = \frac{\sqrt{\epsilon_x \epsilon_z} - \epsilon_3}{\sqrt{\epsilon_x \epsilon_z} + \epsilon_3}, \; k_z = q\sqrt{-\epsilon_x/\epsilon_z}, \; \mathrm{Im}[k_z] > 0$$

are the near field reflection coefficients on the top and bottom surfaces and the z direction wavevector in hBN, q is the in-plane wavevector of the polariton, ϵ_x/ϵ_z is the in-plane/z-direction dielectric of hBN, ϵ_3 is the dielectric of the substrate and d is the thickness of hBN. The dielectric ϵ_3 below the bottom surface is SiO_2. At the typical experimental frequency $1522\ cm^{-1}$, the dielectric of SiO_2 is $\epsilon_3 = 1.29 + 0.009\ i$. Thus the in plane momentum is determined as:

$$dq = \frac{1}{\sqrt{-\frac{\epsilon_x}{\epsilon_z}}}\left(\frac{i}{2}\ln\left(R_{12}R_{23}\right) + \pi N\right)$$

where N is the index of the branch. The SiO_2 contribution to the damping enters through the $\kappa = i \ln\left(R_{12}R_{23}\right)$ factor, which is $\kappa = 1.667(1 + 0.022\, i)$ for the sample made of naturel hBN. If we replace SiO_2 by vacuum, the factor is changed to $\kappa = 1.48(1 + 0.026\, i)$. Therefore, we conclude that SiO_2 contributes only about 0.004 to the total damping factor $Q^{-1} \sim 0.02$ at lowest temperature.

From the phonon polariton dispersion, one can also find the phase and group velocity v_p/v_g. A simpler way to estimate v_g/v_p is to take an infinitely thick sample. For hyperbolic modes in a local medium, this ratio is a function of frequency:

$$\frac{v_{gx}}{v_p x} = \frac{2}{\frac{\partial \ln \epsilon_z}{\partial \ln \omega} - \frac{\partial \ln \epsilon_x}{\partial \ln \omega}}$$

We found $\frac{v_{gx}}{v_p x} \approx 0.076$ at $\omega = 1522\ cm^{-1}$ for bulk polaritons in natural hBN. For slabs, the above equation will not be accurate, especially for the low index branches such as the principle branch $(n = 0)$. This is because the reflection phase shifts among the top/bottom surfaces will modify the polariton group velocity accordingly. Instead, we found $\frac{v_{gx}}{v_p x} \approx 0.039$ for the principle branch in a slab natural hBN based on numerically solving the phonon polariton dispersion. It is also worth to note that here thickness does not affect the ratio in the near field limit due to scale invariance.

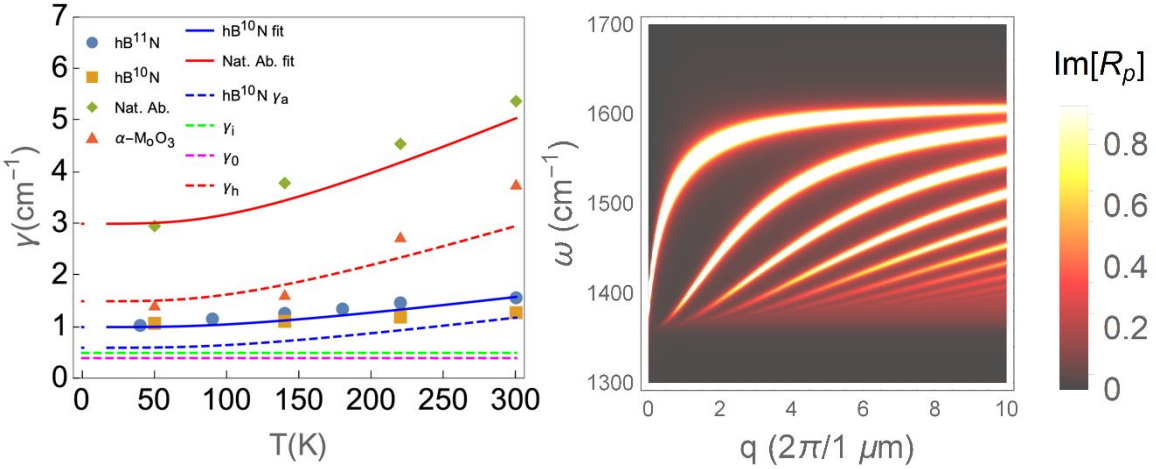

Figure S4 | Left: Phonon polariton damping rate $\gamma = \omega/Q_\omega = \frac{v_g \omega}{v_p Q}$ in the principle branch of hBN and MoO3 devices. Here v_g and v_p are the group and phase velocities. The parameters are: $hB_{11}N$: $\omega = 1522\ \mathrm{cm}^{-1}$, $\frac{v_g}{v_p} = 0.037$; $v_g = 2.28 \times 10^6\ m/s$; $hB_{10}N$: $\omega = 1553\ \mathrm{cm}^{-1}$, $\frac{v_g}{v_p} = 0.039$; natural

hBN: $\omega = 1522\ \mathrm{cm}^{-1}$, $\frac{v_g}{v_p} = 0.039$; α-MoO_3: $\omega = 928\ \mathrm{cm}^{-1}$, $\frac{v_g}{v_p} = 0.039$; The group and phase velocities in α-MoO3 are taken from Ref. [5]. Solid and dashed lines are fittings. **Right:** The calculated near field reflection coefficient of a thick slab made of naturally abundant hBN, indicating the phonon polariton dispersions. The group/phase velocities of the principle (highest) branch can be obtained numerically from this plot.

4. Discussion of phonon polariton damping rate

In this section, we discuss the damping mechanisms of the hyperbolic phonon polaritons in hBN and α-MoO_3 with a focus on hBN. We work under the layer independent approximation while neglecting interlayer coupling except for long range Coulomb interaction that give rise to hyperbolic polaritons. This is a reasonable assumption since the phonon dispersions from exact DFT calculation (Fig. S5a) are nearly flat along the interlayer z direction. Moreover, the lower E_{2g} phonons (anti-phase shear motion of adjacent layers) have a tiny gap and are nearly degenerate with the acoustic phonons.

The temperature dependent part of the damping rate can only be due to temperature dependence of phonon population. Since the highest temperature in our experiment is $T_{room} \approx 300\ K \approx 208\ cm^{-1}$, only the acoustic phonons in hBN are thermally populated and involved during the scattering processes [6]. Accordingly, the symmetry allowed phenomenological model for scattering between hyperbolic polaritons, TO phonons, Raman phonons, impurities, and acoustic phonons reads:

$$H = \sum_k \left(\omega_h(k) h_k^\dagger h_k + \omega_g(k) g_k^\dagger g_k + \omega_a(k) a_k^\dagger a_k\right) + \sum_{k,q} h_{k+q}^\dagger h_k \left(M_{k,q}\left(a_{-q}^\dagger + a_q\right) + V\right) + \sum_{k,q} \mathrm{M}_{g,k,q}\, g_{k+q}^\dagger h_k \left(a_{-q}^\dagger + a_q\right) + c.c.$$

where h_k is the annihilation operator for the hyperbolic polariton with dispersion $\omega_h(k)$, g_k is that for the TO phonons or E_{2g} phonons with a nearly flat dispersion at frequency $\omega_{TO} = \omega_g = 1360\ cm^{-1}$ (at the lower edge of the Reststrahlen band, see Fig. S5a), and a_k is that for acoustic phonons. For simplicity, we assume a single branch of acoustic phonons with isotopic dispersion $\omega_a(k) = v_a k_\perp$.

The anharmonic coupling matrix elements are constrained by inversion symmetry. Note that polartions all belong to the E_{1u} representation which is inversion odd, which is also the case for acoustic phonons. Polaritons can be scattered into each other by emission and absorptions of acoustic phonons with matrix element $M_{k,q}$, or by isotopic impurities with matrix element V. Since the product of two polariton operators is inversion even, the remaining term in the anharmonic coupling must also be inversion symmetric: $\sim \boldsymbol{q} \cdot \boldsymbol{u} \sim q\left(a_{-q}^\dagger + a_q\right)/\sqrt{q}$, rendering the matrix $M_{k,q} = M\sqrt{q}$. The physical picture for this coupling is that acoustic phonons correspond to local strains $\boldsymbol{u}$, which compress/stretch the lattice at the order $\boldsymbol{q} \cdot \boldsymbol{u}$ and thus locally shift the polariton frequency. For isotopic impurities, we assume V is independent of momentum transfer since the impurities lead to atomic mass disorder which acts like short range scattering centers. Polaritons

can also be scattered into TO phonons/E_{2g} phonons by the acoustic phonon with roughly the same matrix element $M_{k,q}$. Note that E_{1u} TO phonons correspond to in-plane electrical dipole moments oscillating at the same phase between adjacent layers in a unit cell, while E_{2g} phonons are out of phase oscillations. Since we neglect atomic interlayer coupling, the scattering matrix elements are the same between them. The actual situation has multiple branches of acoustic phonons, and the scattering matrix elements can depend on the relative directions between the polariton and acoustic phonon momentums. However, they won't affect the qualitatively results, i.e., the frequency and temperature dependence of the polariton damping rates.

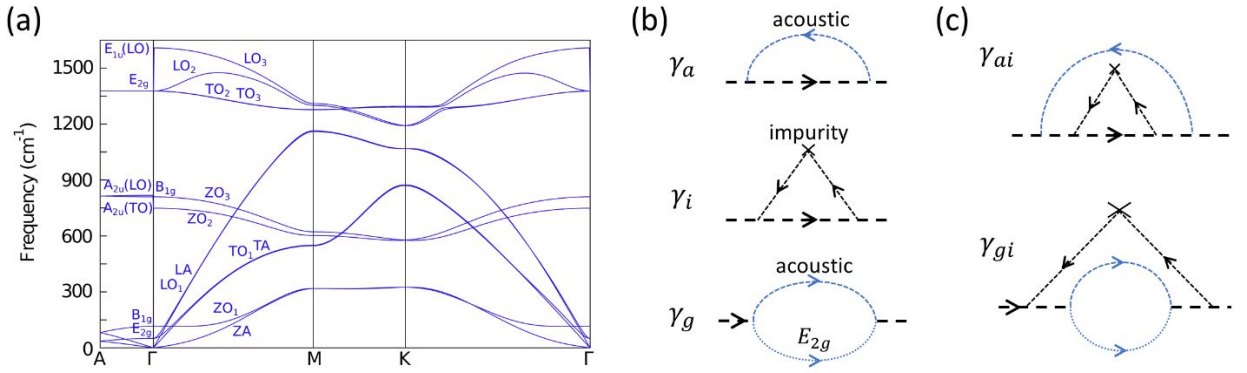

Figure S5. (a) The phonon dispersion in hBN. The hyperbolic polaritons originate from E_{1u} TO and LO phonons and disperse between these two frequencies. (b) The first order self-energies of hyperbolic polaritons (black dashed lines). (c) The second order self-energies.

4.1 First order processes

The first order processes contribute to the self-energies of the hyperbolic polaritons shown in Fig. S5(b), whose imaginary parts are the scattering rates. The polariton with momentum k can be scattered into that at momentum $k' = k + q$, due to emitting/absorbing an acoustic phonon with momentum q, as shown by the top diagram in Fig. S5b. Summing over the final states, one obtains the scattering rate

$$\gamma_a(\omega,T) = \sum_{\boldsymbol{k'}} M^2 q\big(\delta\big(\omega_h(k') - \omega_h(k) - \omega_a(q)\big) n_b(\omega_a(q)) + \delta\big(\omega_h(k') - \omega_h(k) + \omega_a(q)\big)\big(n_b(\omega_a(q)) + 1\big) \big)$$

$$\approx \frac{1}{2\pi}\sum_{k'_x,\, k'_y} M^2 k' \big(2n_b(\omega_a(k')) + 1\big)\frac{1}{v_z(k')}$$

$$\approx M^2 D(\omega)\frac{\Lambda^4}{16\pi^2} 4\int_0^1 dx x^3 (2n_b(T_\Lambda x) + 1)$$

$$\equiv \gamma_{a0}(\omega) f(T/T_\Lambda)$$

where $\gamma_{a0}(\omega) = \frac{1}{16\pi^2} M^2 \Lambda^4 D(\omega)$ is an energy scale, $D(\omega) = \partial_\omega \sqrt{-\frac{\epsilon_x}{\epsilon_z}}$ is the polariton density of states, $T_\Lambda = v_a \Lambda$, $v_z(k) = 1/(k_\perp \partial_\omega \sqrt{-\frac{\epsilon_x}{\epsilon_z}})$ is the z component of the polartion group velocity at momentum k, and Λ is the in plane momentum cutoff for the hyperbolic polaritons (smaller but within the same order of the reciprocal lattice wave vector). Here we have made the approximation that velocities of acoustic phonons are much smaller than those of the polaritons, and the momentum k of the observed polaritons are very close to the Γ point such that $v_a k \ll T, v_a \Lambda$ so it can be set to $k = 0$. We have defined the dimensionless scaling function

$$f(t) = 4\int_0^1 dx x^3 \left(\frac{2}{e^{\frac{x}{t}} - 1} + 1 \right)$$
$$= 1 + \frac{8\pi^4}{15} t^4 + 8t \mathrm{Ln}\left[1 - \mathrm{e}^{-\frac{1}{t}}\right] - 24\mathrm{t}^2 \left(\mathrm{Li}_2\left[e^{-\frac{1}{t}}\right] + 2t\mathrm{Li}_3\left[e^{-\frac{1}{t}}\right] + 2t^2 \mathrm{Li}_4\left[e^{-\frac{1}{t}}\right] \right)$$

where $\mathrm{Li}_n[x]$ are Polylogarithm functions. It has simple expressions in low and high temperature limits: $f(t) = \frac{8\pi^4}{15} t^4 + 1$ at $t \ll 1$ and $f(t) = \frac{8}{3} t + 1$ at $t \gg 1$.

Impurities cause similar process of scattering, as shown by the middle panel of Fig. S5(b), but leads to a temperature independent scattering rate:

$$\gamma_i(\omega) \approx \sum_{k_x', k_y'} V^2 \frac{1}{v_z(k')} \approx \frac{1}{6\pi} V^2 D(\omega) \Lambda^3.$$

We now compute the rate of decay of a polariton at $k = 0$ into E_{1u} TO or E_{2g} phonons by emitting acoustic phonons (bottom panel of Fig. S4(b)):

$$\gamma_g(\omega, T) = \sum_q M^2 q \delta(\omega - \omega_{TO} - v_a q)(n_b(v_a q) + 1)$$

where c is the hBN out of plane lattice constant and we has defined the frequency scale γ_{g0}. Since the involved acoustic phonon energy $\omega - \omega_{TO} \approx 160\ cm^{-1}$ is lower than room temperature $T_{room} \approx 208\ cm^{-1}$, this process can also lead to substantial temperature dependence.

4.2 Higher order processes

We now discuss the higher order processes involved terms like $\gamma \sim V^4, M^4, V^2 M^2$. The experimental results shown in Fig. S4 clearly indicates that the natural abundance hBN has a substantially faster temperature dependence than isotopically pure hBN. One plausible explanation for the differences comes from a scattering process involves both impurities and acoustic phonons. For this the most natural event is the second order process where the polariton is scattered from k to k' by an acoustic phonon, and then to k'' by impurities, and vice versa. For simplicity, we compute the scattering rate in the case of $T \gg v_a \Lambda$:

$$\gamma_{ai}(\omega,T) \approx \gamma_a(\omega,T)V^2\Lambda^3\int_{\omega_{TO}}^{\omega_{LO}} d\omega' \frac{D(\omega')}{(\omega'-\omega)^2} = \frac{1}{\omega_{ai}}\gamma_i(\omega)\gamma_a(\omega,T)$$

$$\gamma_{ii}(\omega) = \frac{1}{\omega_{ai}}\gamma_i^2(\omega)$$

where $\omega_{ai} = D(\omega)/\int_{\omega_{TO}}^{\omega_{LO}} d\omega' \frac{D(\omega')}{(\omega'-\omega)^2}$ is a frequency scale. Since the integral has infrared divergence, this ω_{ai} is likely to be small such that γ_{ai} becomes important. If infinite higher order processes are summed over, the infrared divergence disappears. An example is impurity induced scattering rate of electrons where summing over no-crossing diagrams gives the Born approximation. Another second order process is that the polariton is firstly scattered into another polariton by impurities, and then scattered into a E_{2g} phonon by an acoustic phonon. The corresponding scattering rate is

$$\gamma_{aig}(\omega,T) \approx \gamma_g(\omega,T)V^2\Lambda^3\int_{\omega_{TO}}^{\omega_{LO}} d\omega' \frac{D(\omega')}{(\omega'-\omega)^2} = \frac{1}{\omega_{ai}}\gamma_i(\omega)\gamma_g(\omega,T)$$

We subsume these temperature dependent contributions using

$$\gamma_{\mathrm{h}}(\omega,T) = \gamma_{ai}(\omega,T) + \gamma_{aig}(\omega,T) = \kappa_{\mathrm{i}}(\omega)\big(\gamma_a(\omega,T) + \gamma_g(\omega,T)\big)$$

and absorb the temperature independent one γ_{ii} into γ_i. Moreover, the nonzero residual scattering rate in the low temperature limit of isotopically pure hBN suggests that there exist processes [6, 8] that does not involve acoustic phonons, which we set as a fitting parameter γ_0.

4.3 Total scattering rate

The total scattering rates for natural and isotopically pure hBN are

$$\gamma_{iso}(T) = \gamma_0 + \gamma_a(T) + \gamma_g(T), \quad \gamma_{\mathrm{natural}}(T) = \gamma_{iso}(T) + \gamma_i + \gamma_{\mathrm{h}}(T)$$

where γ_0 is a temperature independent scattering rate due to other decaying processes[2]. The dashed lines in Fig. S3 correspond to $\gamma_0 = 0.4\ cm^{-1}, \gamma_{a0} = 0.6\ cm^{-1},\ \gamma_g = 0, \gamma_i = 0.5\ cm^{-1}, \kappa_{\mathrm{i}} = 2.5$ and $T_\Lambda = 450\ K$. Note that these are fitting parameters and their more accuate values is a theoretical question that awaits to be addressed by first principle calculations.

References:

1. Z. Fei, et al. Gate-tuning of graphene plasmons revealed by infrared nano-imaging. Nature 487 82 (2012).
2. S. Dai et al. Tunable phonon polaritons in atomically thin van der Waals crystals of boron nitride. Science 343, 1125-1129 (2014).
3. Ni, G. X. *et al*. Fundamental limits to graphene plasmonics. *Nature* **557**, 530-533 (2018).

4. S. S. Sunku et al. Photonic crystals for nano-light in moire graphene superlattices. Science 362, 1153-1156 (2018).
5. W. Ma et al, Nature volume 562, 557–562(2018).
6. R. Cuscó et al, Phys. Rev. B 97, 155435 (2018).
7. Sun, Z., Gutiérrez-Rubio, Á., Basov, D. N. & Fogler, M. M. Hamiltonian Optics of Hyperbolic Polaritons in Nanogranules. Nano Letters 15, 4455-4460, (2015).
8. Alfredo Segura, Ramon Cuscó, Takashi Taniguchi, Kenji Watanabe, and Luis Artús, Phys. Rev. B 101, 235203